SANDIA REPORT
SAND2007-1734
Unclassified Unlimited Release
Printed April 2007

Overview of the Dynamic-Hohlraum X-ray Source at Sandia National Laboratories

Thomas W. L. Sanford

Prepared by
Sandia National Laboratories
Albuquerque, New Mexico 87185 and Livermore, California 94550

Sandia is a multiprogram laboratory operated by Sandia Corporation,
a Lockheed Martin Company, for the United States Department of Energy's
National Nuclear Security Administration under Contract DE-AC04-94AL85000.

Issued by Sandia National Laboratories, operated for the United States Department of Energy by Sandia Corporation.

Available to DOE and DOE contractors from
U.S. Department of Energy
Office of Scientific and Technical Information
P.O. Box 62
Oak Ridge, TN 37831

Telephone: (865) 576-8401
Facsimile: (865) 576-5728
E-Mail: reports@adonis.osti.gov
Online ordering: http://www.osti.gov/bridge

Available to the public from
U.S. Department of Commerce
National Technical Information Service
5285 Port Royal Rd.
Springfield, VA 22161

Telephone: (800) 553-6847
Facsimile: (703) 605-6900
E-Mail: orders@ntis.fedworld.gov
Online order: http://www.ntis.gov/help/ordermethods.asp?loc=7-4-0#online

SAND2007-1734
Unclassified Unlimited Release
Printed April 2007

Overview of the Dynamic-Hohlraum X-ray Source at Sandia National Laboratories

Thomas W. L. Sanford*
Diagnostics & Target Physics Department
Sandia National Laboratories
P.O. Box 5800
Albuquerque, NM 87185-0958

Abstract

Progress in understanding the physics of Dynamic-Hohlraums is reviewed for a system capable of generating 10 TW of axial radiation for high temperature (>200 eV) radiation-flow experiments and ICF capsule implosions. 2D magneto-hydrodynamic simulation comparisons with data show the need to include wire initiation physics and subsequent discrete wire dynamics in the simulations if a predictive capability is to be achieved.

* Invited paper given at the *2006 International Conference on Megagauss Magnetic Field Generation and Related Topics*, November 10, 2006 Santa Fe, New Mexico, USA.

Acknowledgements

This research was done in close collaboration with many of my colleagues at IC, ITEP, LANL, NRL, SNL, and UNM, including Drs. J. A. Apruzese, D. E. Bliss, J. P. Chittenden, M. E. Cuneo, M. G. Haines, C. A Jennings, R. J. Leeper, T. J. Nash, D. L. Peterson, G. A. Rochau, N. F. Roderick, S. E. Rosenthal, G. S. Sarkisov, P. V. Sasorov, and W. A. Stygar. I would like to thank Dr. R. J. Leeper for sustained programmatic support, R. C. Mock for timely data processing and for generating the exquisite graphics, T. L. Cutler for her technical editing, Drs. William A. Stygar and Mary Ann Sweeney for carefully reviewing this article, and Dr. Isaac Eliaz MD for enabling me to complete this research.

Table of Contents

I. INTRODUCTION

Dynamic-hohlraums (DHs) [1-4] driven by a wire-array z-pinch are being developed and used as intense blackbody x-ray sources for inertial-confinement-fusion (ICF) [5-9] and high-temperature radiation-flow experiments [10-11] (Fig. 1). DHs are currently the most energetic and intense pulsed-power-driven sources available in the laboratory for these applications [12-13].

In the baseline DH developed at Sandia National Laboratories [14-15] (Fig. 2), two concentric cylindrical arrays of tungsten wires are used to form an imploding z-pinch-plasma shell. The shell generates x-rays as it impacts a low-opacity cylindrical target made of low-density foam that is centered on the z-pinch axis [16]. The shock wave produced by this collision transfers a portion of the kinetic energy of the pinch implosion to internal and radiative energy within the foam. As the tungsten wires ablate, merge, and implode, the resulting high-atomic-number plasma functions as a hohlraum, trapping radiation within.

In ICF experiments, x-rays interior to the DH are used to directly implode ICF capsules (Fig. 1) centered on the z-axis [7-9]. In radiation-transport experiments, x-rays exiting a top radiation-exit-hole (REH) (Fig. 1C) are used to study radiation flow at temperatures exceeding 200 eV [10]. X-rays exiting a bottom REH are used to monitor the radiation exiting the top when diagnostic access to the top is not available [11]. X-rays exiting the top REH of one DH and the bottom of a second DH (as illustrated by Fig. 1A) could be used to indirectly implode an ICF capsule [5,16], as in Olson's static-wall-hohlraum concept [17]. Implicit in these applications is the assumption that the axial radiation produced is top-bottom symmetric [18].

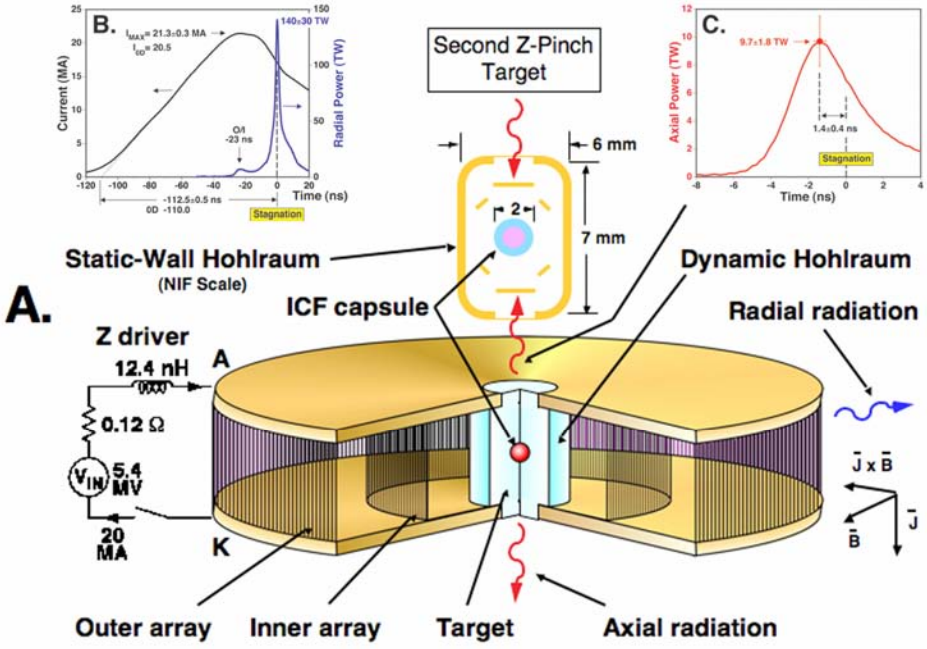

Figure 1. (A) Approximate Z circuit driving dynamic hohlraum load, showing position of outer array, inner array, foam target, ICF capsule and static-wall hohlraum. (B) Measured current and radial radiation power. (C) Measured axial radiation power from top 2.4-mm diameter radiation exit hole.

Sandia's initial DH configuration was developed by Nash and colleagues [3], after it was established that a high x-ray power could be generated by a wire-array z-pinch if a large number of wires were used in the array [19-20]. This configuration, like the present arrangements [10,14-15], consisted of two coaxial nested arrays (Fig. 2) where the diameter Φ and wire number N of the outer array were 40 mm and 240 wires, respectively. The inner array

was half the diameter of the outer, the inner wire number was half that of the outer, and the mass of the inner was half of the outer. The mass of the central foam target was equal to the sum of the masses of the inner and outer arrays. Since the initial use of this DH as a routine ICF and radiation-flow platform, several experimental series were performed using the generic arrangement of Figs. 1 and 2 to understand the underlying dynamics of the implosion and its subsequent x-ray generation.

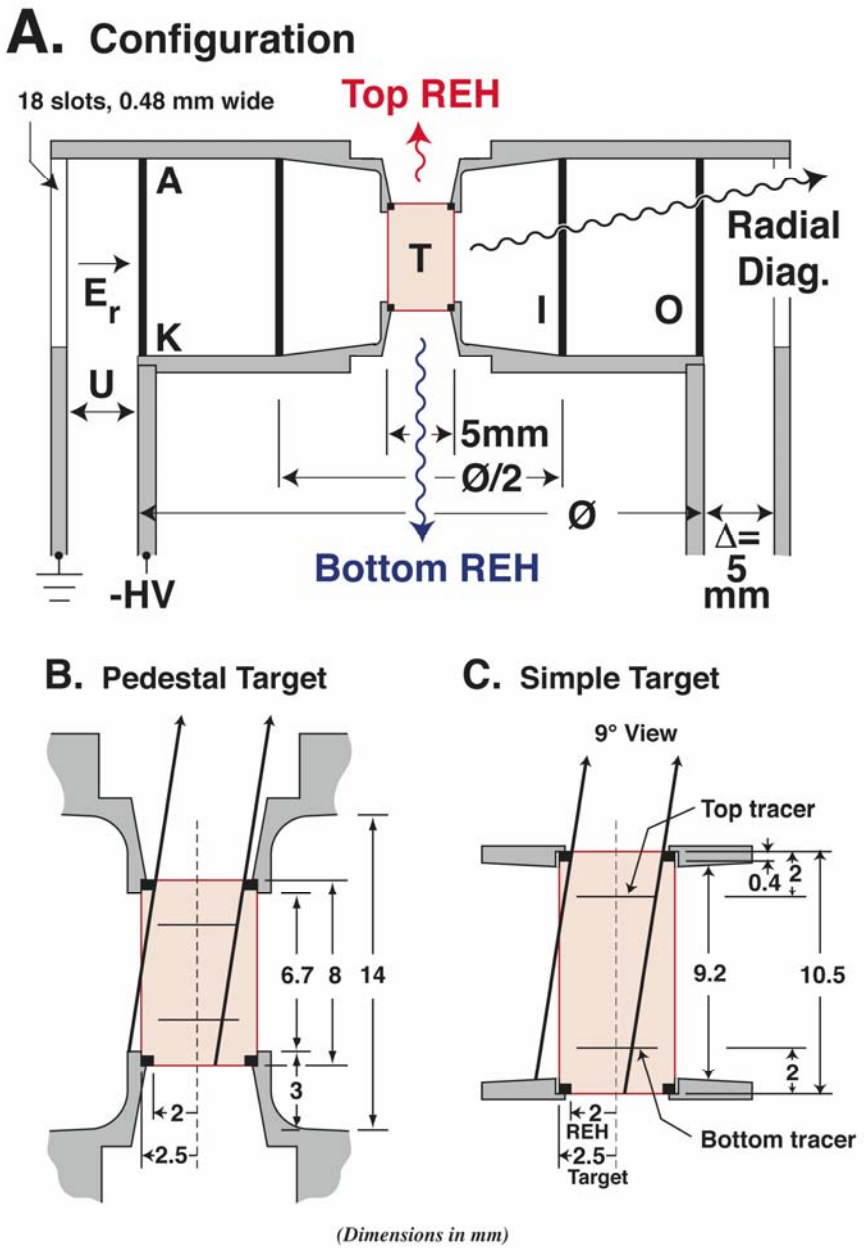

Figure 2. (A) Experimental arrangement showing position of target (T), inner (I) and outer (O) arrays, and top and bottom radiation exit holes (REHs), together with the general diagnostic layout. (B) Pedestal target. (C) Simple target.

In this paper, we review the results of these experimental series together with associated numerical simulations. It is a testament to the work of Nash [3] that the initial configuration described in Ref. [3] closely maximizes the axial

power, and thus has become our baseline configuration.

Until recently, DH simulations have been limited to one or two dimensions in the r-z or r-θ plane. The simulations assume that the dynamics can be described by radiation [21-23] or resistive [24-25] magneto-hydrodynamic (MHD) approximations. To date the simulations have ignored the physics of the transition from the initial energy deposition in the wires, to wire ablation, and subsequently, to wire-plasma merger, during which a plasma shell forms and implodes [26-28]. The simulations generally start the implosion with the assumption that a plasma shell forms early in time. Detailed comparisons with the data discussed here, however, show the need to include wire-ablation physics in order to achieve a genuine predictive capability.

The paper follows the power flow through the implosion (Fig. 1), providing first a brief overview of the coupling between the Z generator and the DH. The optimization of the outer array is discussed next, followed by the development of the collision between the outer and inner arrays, the optimization of the target length, the development of the shock within the target, the description of the radiation exiting the top REH, and an explanation of the measured top-bottom axial radiation asymmetry.

Central to many applications of the DH is the symmetry of its axial radiation. As such, this issue is discussed in depth in the last sections of this review. Importantly, the paper discuss the mystery behind why increasing the mass of the outer array diminishes axial x-ray power [29], why the addition of the inner array only marginally increases the axial x-ray power [29], and why a significant difference exists in the axial radiation exiting the top REH relative to that exiting the bottom [18]. These observations, which are all in contrast to the predictions of MHD simulations, are shown in this article to be related to the discrete nature of the wires, and in the last case, to the large radial electric field on the surface of the outer array of wires before the plasma-shell forms [30].

II. Z GENERATOR AND DH LOAD OVERVIEW

The Z [31] generator and DH load form a coupled system, where the generator can be viewed as a high-voltage source in series with the source impedance (0.12 Ohm) and the inductance (~12.4 nH) of the vacuum-section transmission lines (Fig. 1A). The L/R current rise time of this system is ~100 ns. As current flows through the load (Fig. 1B), initially a plasma shell forms only in the outer array O, since little current flows through the higher-inductance inner array I (Fig. 2A) [24]. As the outer current-carrying shell implodes towards the axis, however, the inductance rises and the current flow becomes restricted (Fig. 1B). For the baseline configuration (Φ = 40 mm and N = 240) with a simple target (Fig. 2C), the outer array O collides with the inner I at -23 ns, which produces the radial radiation peak [10] at -23 ns shown in Fig. 1B. After the O/I collision, the two arrays continue to implode more or less together, impacting the target at about -6 ns and stagnating on axis at 0 ns. Stagnation is defined experimentally as the time when the radial power reaches its maximum (140±30 TW) [10], as shown in Fig. 1B.

The associated axial radiation exiting the top REH (which has a 2.4-mm diameter) is illustrated in Fig. 1C. It peaks at -1.4±0.4 ns with a power of 9.7±1.8 TW [10]. The measured implosion time of 112.5±0.5 ns is in reasonable agreement with the 110 ns modeled by the SCREAMER transmission-line model [32] (Fig. 1B), and the estimated L/R rise time of 100 ns. Here as elsewhere in the paper, the uncertainties generally are the 1σ values of random shot-to-shot fluctuations, and time t=0 is defined to be when the radial power reaches its peak value.

III. OUTER ARRAY OPTIMIZATION

Recently, variations in the baseline arrangement, keeping the above implosion time fixed, have been made to determine if this coupled system produces close to maximal

radiation power. One variation (Table I) changed the outer array diameter Φ from 24 to 56 mm in five discrete steps by keeping the product of the load mass times the square of the load diameter fixed (which holds the implosion time constant). In this procedure the inner array was kept at half the diameter of the outer, the inner wire number was kept at half that of the outer, and the mass of the inner was kept at half the outer. The mass of the central foam target was kept equal to the sum of the inner and outer arrays (Table I). These constraints were shown earlier to maximize approximately the radiated x-ray power for a 40-mm outer array diameter [3,33]. As discussed in Section VIIIA, wire-array tungsten plasma is observed to flow prematurely across the REHs when the simple target (Fig. 2C) is used. To eliminate this early time tungsten, which absorbs and reduces the radiation generated from the hohlraum interior exiting the REHs, the pedestal target (Fig. 2B) was used in the optimization. Additionally because power has been shown to depend on wire number [19-20,34-35], for each diameter, wire number changes were kept within about ± 15 % of the mean number of wires used (Table I).

Table 1. Shot Configurations

Shot type	Array Ø (mm)	Wire #	Wire Ø (mm)	Wire mass (mg/cm)	Target density (mg/cc)	Target mass (mg/cm)	Z shot #	E_r
Baseline	40/20	240/120	7.5/7.5	2/1	14	3.0	1132, 1244 1246, 1248 1598, 1664	1
MR^2	56/28	288/144	5/5	1.06/0.53	7.5	1.6	1659, 1662	1.75
	48/24	240/120	6.3/6.3	1.4/0.7	10	2.1	1600, 1663	1.43
	32/16	256/128	8.9/8.9	3.0/1.5	21	4.5	1660, 1665	0.63
	24/12	332/166	10/10	5.0/2.5	34	7.5	1661, 1666	0.33
Wire #	40/20	540/270	5/5	2/1	14	3.0	1715	0.67
	40/20	360/180	6.1/6.1	2/1	14	3.0	1667	0.82
	40/20	172/86	8.9/8.9	2/1	14	3.0	1716	1.18
	40/20	108/54	11.2/11.2	2/1	14	3.0	1717	1.49
Reverse mass	40/20	240/120	5.2/10.5	1/2	14	3.0	1245, 1247	1.44

The shot sequence was motivated by 1D resistive-MHD simulations [33] that suggested the axial power could be increased by reducing the load diameter, as illustrated by Fig. 3A. Specifically, the simulations show the axial power should have a broad maximum near 28 mm, improving the power output by ~50% from that calculated at 40 mm. At diameters greater than 40 mm, the calculated implosion velocity onto the foam target exceeds 0.6 mm/ns. Subsequently the radiating shock wave in the foam (the DH heating source) is also very fast, too fast for the electrons in the shock to couple efficiently to the radiation. As the diameter is decreased below 40 mm, the electrons and radiation in the shock wave couple efficiently and equilibrate. Additionally, as the diameter decreases, the total mass of the wire-arrays increases (to keep the implosion time fixed) and the optical trapping of the arrays increases, which also increases the axially radiated power.

Below an outer-array diameter of 28 mm, however, the simulations show the axial power falling. Below this diameter the velocity of the imploding wire arrays is less than 0.42 mm/ns and the mass of the foam becomes a substantial energy sink. Much of the kinetic energy of the implosion is invested in internal energy of the foam, and the radiated power falls. The simulations indicate that in this regime, however, the axially radiated power may still be recovered by reducing the foam mass [33].

In contrast to these expectations, both the measured axial and radial powers fall below ~40 mm (Figs. 3A and 3B). At a diameter of 28 mm, the predicted axial power is four times higher than that measured (Fig. 3A). The difference likely lies with the details of the wire-array dynamics not included in the simulations, and in particular the generation of trailing mass as the

array mass is increased at these lower array diameters [27,36]. Additionally, the power exiting the bottom REH gradually decreases relative to the top as the diameter increases. This departure from axial up-down radiation symmetry is discussed in Section VIII, and will be shown to depend on the negative radial electric field E_r at the surface of the outer wire array (Fig. 2A), which decreases as the diameter decreases [30].

As might be expected, the measured radial power (Fig. 3B) tracks the axial power (Fig. 3A), also peaking at a diameter of 40 mm.

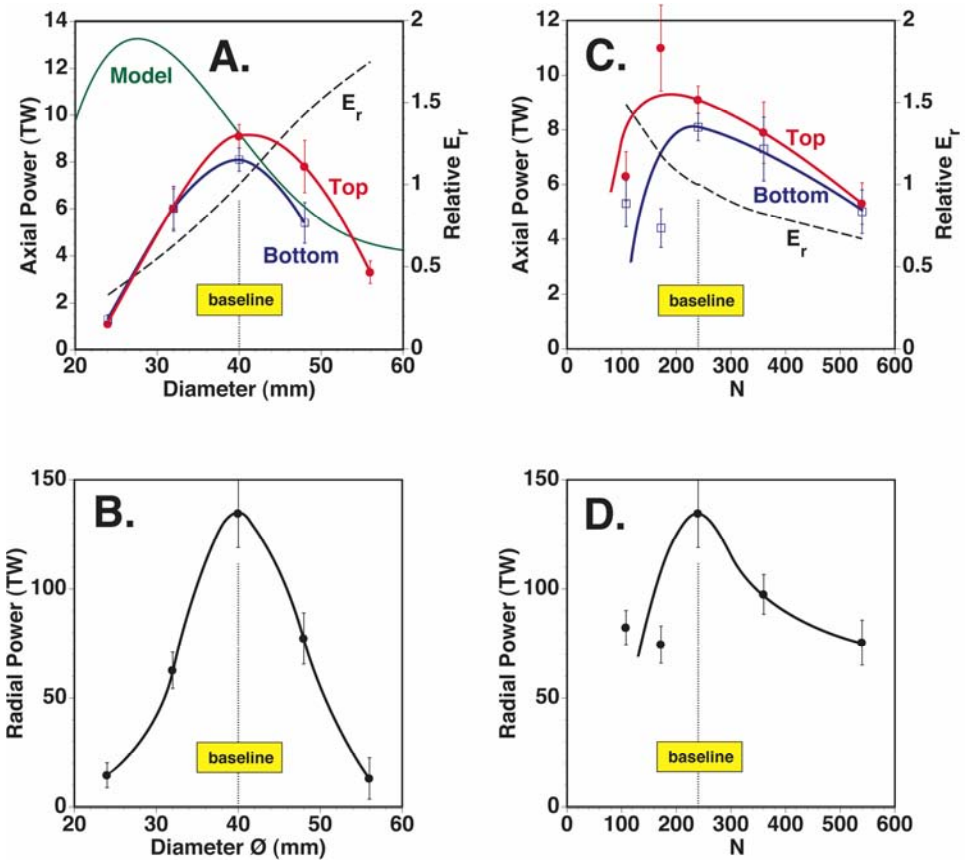

Figure 3. (A) Measured and modeled axial power and associated relative radial electric field (E_r) at surface of outer wires as a function of outer array diameter (Φ). (B) Measured radial power as a function of Φ. (C) Measured axial power as a function of outer array wire number (N). (D) Measured radial power as a function of N.

The other variation explored changed the outer-array wire number N from 108 to 540 in 5 discrete steps, keeping the outer-array mass the same at 2 mg/cm (Table I). As above, it used the pedestal target (Fig. 2B), and the inner array was kept at half the diameter of the outer, the inner wire number was kept at half that of the outer, and the mass of the inner was kept at half the outer. The mass of the central foam target was kept equal to the sum of the masses of the inner and outer arrays.

Like the previous scan, the data suggest that the baseline, with 240 outer-array wires, maximizes both the radial and axial radiated powers (Figs. 3D and 3C). As the number of wires decreases the bottom power begins to depart from that of the top (Fig. 3C). As with the departure from axial radiation symmetry observed with the diameter variation (Fig. 3A), Section VIIIB will show that the asymmetry is strongly correlated with E_r, which decreases as N increases [30]. The increase in power with increasing wire number (and decreasing inter-wire spacing), in contrast, is related to the transition from the implosion of individual wire plasmas to that of a plasma shell where the wire coronas have merged and to the increased

azimuthal symmetry of the merging coronas [19,20].

The decrease in power for very large wire numbers, however, is not understood. Several mechanisms have been proposed [34]. These include the onset of wire-core merger where the instability modes become correlated and the amount of stabilizing precursor plasma is therefore reduced, to a lower dI/dt per wire [37], which may generate increased variation in the individual wire energy deposition.

As shown in Figs. 3A and 3B, the radial power (Fig. 3D) peaks at the axial power maximum (Fig. 3C).

IV. OUTER-INNER ARRAY COLLISION

2D simulations in the r-z plane suggest that the addition of the inner array would increase the axial power by a factor of ~2-3 (Fig. 4A) [29]. The simulations assume that by the time of the O/I (outer/inner) collision both arrays have formed azimuthally symmetric plasma shells and that the collision is hydrodynamic; namely, that the two arrays stick together after the collision. The magnitude of the initial seed used for the development of the magneto-Rayleigh-Taylor (MRT) instability is that which provides agreement with the measured axial radiation power when the inner array is present. The substantial increase in power with the nested configuration results from resetting the growth of the MRT instability that develops in the outer array by the time of the O/I collision. Measurements show, however, that the addition of the inner array increases the axial power by only 23±15% (Fig. 4B), with a similar increase in radial power [29]. The reduced improvement suggests that the MRT instability may be less significant than calculated. By reducing the magnitude of the MRT seed a factor of four, the power difference between the two configurations simulated can indeed be brought into agreement with the data as illustrated in Fig. 4C. In this case, however, the overall powers are ~20% higher than those measured, and the predicted radial powers are even less consistent with those measured [29].

These inconsistencies have been recently resolved in an experiment in which the outer and inner masses of the baseline DH configuration were reversed to determine if the assumption of a hydrodynamic collision is justified. Reversal allows the assumption of a hydrodynamic collision to be differentiated from that of a more transparent collision [38]. Figs. 5A and 5B illustrate expected differences in timing characteristics of the x-ray radiation pulse between the two modes, when the masses are reversed. The figures show the evolution of the average radius of the arrays using the 0D discrete-wire thin-shell model of Waisman and Cuneo [39-41].

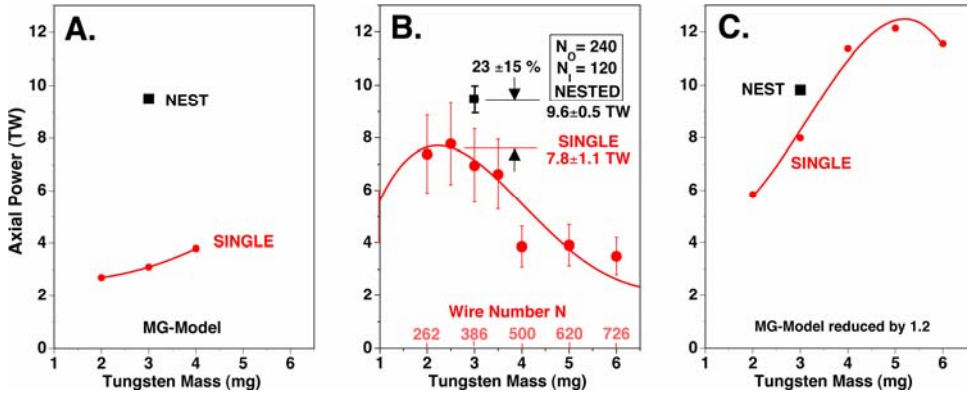

Figure 4. Axial power (A) simulated in the r-z plane, (B) measured, and (C) simulated in the r-z plane with an initial perturbation level four times smaller than that used in (A).

In the case of a hydrodynamic collision (Fig. 5A), a radiation pulse is anticipated when the outer array collides with the inner (O/I) at 200 ns, as well as at 222 ns when the combined arrays collide with the target ([O+I]/T). When the collision is more transparent, again a

radiation pulse is anticipated at the O/I collision, but now *two* subsequent signals are expected: the first when the former outer array collides with the target (O/T) at 213 ns, and the second when the former inner collides with the target (I/T) at 227 ns (Fig. 5B). These later features are seen in r-θ resistive-MHD simulations [25] of the reversed mass configuration, as well as experimentally (Fig. 5C), thus suggesting this O/I collision is transparent-like [38]. Timing between the associated events in the 2D model is foreshortened because the inductive loading of the load is not included, and therefore cannot be used to provide an accurate measure of timings. The timing difference calculated in the 0D model, however, can be used. This model incorporates the inductive loading. In this model, the calculated time difference between the O/I and O/T signals of 13 ns is in excellent agreement with the 14 ns measured (Fig. 5D), assuming very little momentum is transferred from the outer array to the inner (*ie* that the collision is essentially transparent) [38]. To facilitate the comparison in Fig. 5C, the timing of the simulated O/I signal has been adjusted to coincide with that measured at -31 ns.

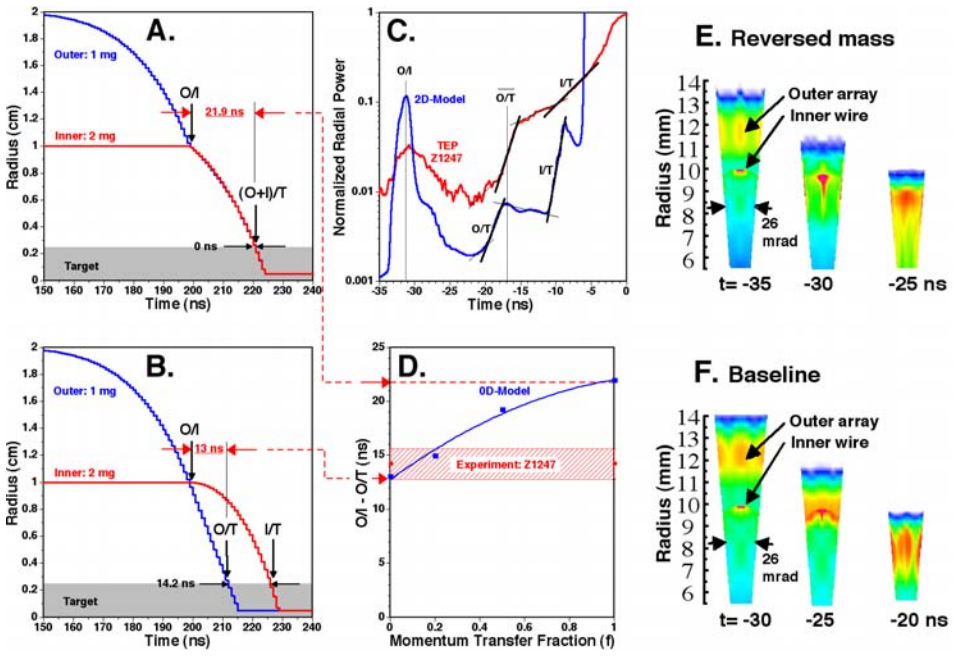

Figure 5. Calculated trajectories of the outer and inner wire arrays assuming O/I collision is (A) hydrodynamic and (B) transparent. (C) Measured and simulated radial power. (D) Comparison of measured time difference (O/I-O/T) with that calculated as a function of momentum transferred at the O/I collision. Simulated implosion in the r-θ plane for (E) reversed mass and (F) baseline configuration.

In the experiment all parameters such as wire number, array radii, and the target mass and geometry remained the same, except that the diameters of the individual wires were adjusted to reverse the array masses. This meant reducing the outer wire diameter from 7.4 to 5.2 μm, and increasing the inner wire diameter from 7.4 to 10.5 μm. In this case, the ratio of the inner wire gap to wire diameter changes by only ±30%, and little difference in the dynamics of the collision between the baseline and reversed-mass configuration is expected.

This expectation is born out in the 2D simulations (Figs. 5E and 5F). These r-θ simulations show that the outer array forms a plasma shell prior to the O/I collision in either configuration. At this time, the inner array still remains as a discrete array of wire plasmas, with the bulk of the current flowing in the lower-inductance outer shell. The current switches to the inner array once the outer shell passes through the inner array. Because the O/I collision in the reverse-mass mode is clearly transparent (Figs. 5C and 5D) and because the

simulations show the underlying dynamics to be similar between the two configurations, the O/I collision in the baseline configuration is thus also transparent. Hence the transparent nature of the collision likely explains the minimal effect that the addition of the inner array has in mitigating MRT in the outer array.

Although the collision is clearly not hydrodynamic, the measured wavelength of the measured MRT instability both before and after the collision in the r-z plane is in excellent agreement with that simulated by the r-z radiative-MHD model [38]. With significant features observable in both the r-z as well as the r-θ plane, these results illustrate the 3D nature of the O/I collision.

The lack of agreement between Fig. 4B and Fig. 4C at the high mass of 6 mg illustrates another mystery resolved by the lack of discrete wire dynamics in the simulations. Namely, the 2D simulations (Fig. 4C) predict the axial power to increase by ~50% when the mass of the single outer array doubles from 3 to 6 mg [29]. The increase results from improved radiation trapping due to the thicker tungsten shell and to reduced MRT growth. In contrast to the prediction, the measurements show that the axial power actually decreases by more than a factor of two. The mystery is understood by the data of Figs. 3C and 3D, which show that a significant decrease in radiated power arises when the wire number is increased beyond 240. The masses of arrays used in the experiments of Fig. 4B were increased by systematically increasing wire number, nearly doubling the number of wires from 386 to 726 (Fig. 4B). Thus again like the inner wire transparency, the discrete nature of the wire dynamics needs to be included in the modeling if meaningful predictive capability is to be achieved.

V. TARGET LENGTH OPTIMIZATION

Figure 6 illustrates the measured top axial power as a function of target length for the baseline configuration, showing a clear maximum near 8 mm [42]. For these measurements, the simple target of Fig. 2C was used. The diameter of the top REH was 2.4 mm. The bottom REH was not present. In this experiment only the length of the target and associated anode-cathode (AK) gap (*ie* the distance between the upper and lower pinch electrodes) was changed; the target mass per unit length and target foam diameter remained fixed at 3 mg/cm and 5 mm, respectively. Shown also in Fig. 6 are results of the 2D radiative-MHD simulation [21-23] in the r-z plane [42].

Because the optical depth of the bulk radiation generated is only a few mm [43], the axial power is expected to increase with decreasing length, as the kinetic energy (KE) per unit length increases. Above 8 mm this expectation is born out; the rapid fall-off in power below 7 mm, however, was unexpected. The power decrease is now understood to be due to early generation of wire-array tungsten plasma, flowing close to the electrode walls and disrupting the axial coherence of the plasma shell. Measurements suggest the disruption may extend as much as 3 mm above or below the cathode or anode surface, [43] and is related to the axial radiation asymmetry discussed in Section VIII. The power decrease may also be caused, in part, by closure of the AK gap defined by the upper and lower pinch electrodes by trailing mass that shunts the current at large radii [27,36].

VI. SHOCK FORMATION IN THE TARGET

Figure 7A illustrates the development of the mass-driven shock from the impact of the wire arrays on the pedestal target (Fig. 2B), simultaneously measured from both REHs. The measured radii inferred for the shock converge toward the z-axis reasonably symmetrically [15]. The enhanced emission on axis prior to the arrival of the main shock (at about -4.5 ns) is consistent with the existence of a radiation-driven shock in the foam target. Calculations indicate this shock forms from radiation generated when the outer wire-array plasma impacts the inner array of the nest (-23 ns in Fig 1B) [15].

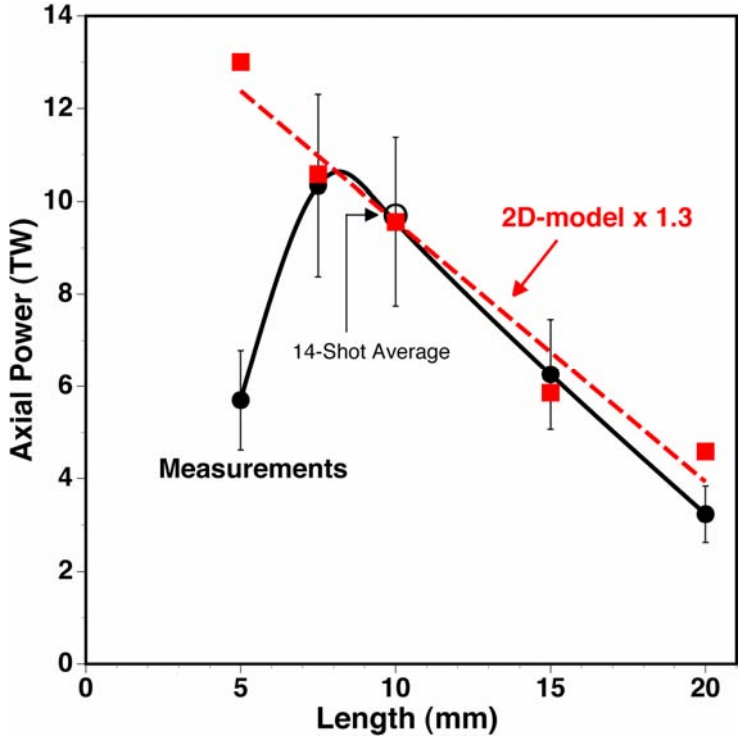

Figure 6. Measured and simulated top axial power as a function of target length.

The mass-driven shock at early time (-7 ns) exhibits an 18-fold variation in brightness (Figs. 7A and 7B) suggestive of the initial 18-slot structure in the current return can (Fig. 2A). With time, the structures coalesce, with the variation in brightness diminishing (Figs. 7B and 7C). The variations coalesce earlier (Fig. 7B) and retain larger swings in the simple target (Fig. 2C) relative to those measured with the pedestal target. Moreover the rise-time of the axial radiation, the shot-to-shot variation in the axial-radiation pulse shape, and the measured shock velocity [15] of the pedestal target all decrease relative to the simple target. These results suggest that the quality of the plasma shell, which forms within the central region of the implosion, is superior to that adjacent to either electrode. The above observations are consistent with the unexpected decrease in axial emission for targets lengths below ~ 7 mm (Fig. 6) where the central region is diminished relative to the 3-mm edge regions.

The brightness variation of the shock is consistent with resistive MHD simulations in the r-θ plane [44]. They show that the effect of the slotted can is manifest in a redistribution of outer-array-plasma mass in azimuth, with a period equal to the slotted-can period, which survives to impact with the target. Specifically, the slots generate an 18-fold perturbation level of a roughly sinusoidal ±10% variation in magnetic field adjacent to the wires of the outer array. The principal effect of the variation is to focus the wire precursor flows so that they converge off-axis, also with 18-fold symmetry. Later, when the implosion of the subsequent plasma shell starts, the shell then follows this imposed structure, resulting again in an azimuthally focused flow which persists after impacting the foam.

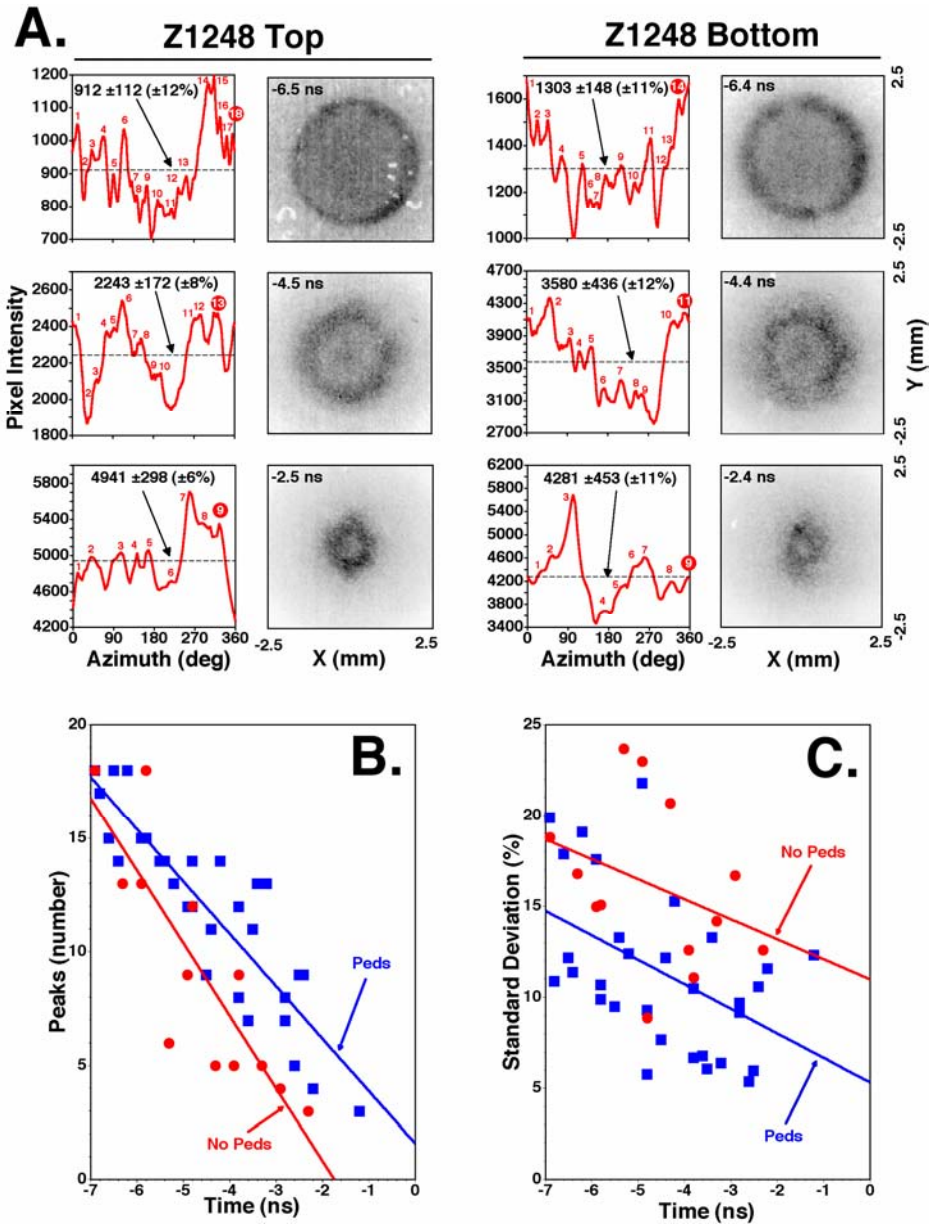

Figure 7. (A) Measured shock images in the target as a function of time as viewed from top and bottom REHs. Associated azimuthal lineouts of the shock are shown adjacent each image. (B) Number of peaks measured in the lineouts and (C) RMS standard deviation of the intensity variation around lineouts as a function of time.

VII. TOP AXIAL RADIATION

Figure 8 illustrates the spectral content of the top axial power [10] measured with the baseline configuration using a simple target (Fig. 2C). At peak power, the radiation can be characterized by that of a Planckian distribution having a temperature of ~230 eV, together with a high-energy tail, as illustrated in Fig. 8A for Shot Z571. The tail may be associated with a non-thermal electron source. It represents ~6% of the power above 1.5 keV. Figure 8B shows the time evolution of the spectrum measured between 1.4 and 2.4 keV [15]. For these measurements, Al and Mg tracers were embedded 2 mm in from either REH, within the target (see insert in Fig. 8B). Figure 8C compares the associated spectroscopic temperature [45,46] extracted from the ratios of the Al, He, and H emission and absorption lines

(Fig. 8B) [15], the color temperature extracted from the shape of the Planckian between 1.4 and 2.4 keV (Fig. 8B) [15], and the brightness temperature extracted from shock images (like those of Fig. 7A) and simultaneous power measurements [15].

The measurements support an internal hohlraum temperature of ~230 eV at peak axial power. The color temperature is systematically higher than the other two measurements, likely because the keV emission is able to escape from deeper (*i.e.*, more central and hotter) regions of the hohlraum. Radiation leakage from the REH cools the outer few mm of the hohlraum. Here the temperature is measured to be ~50 eV lower than in the interior [47].

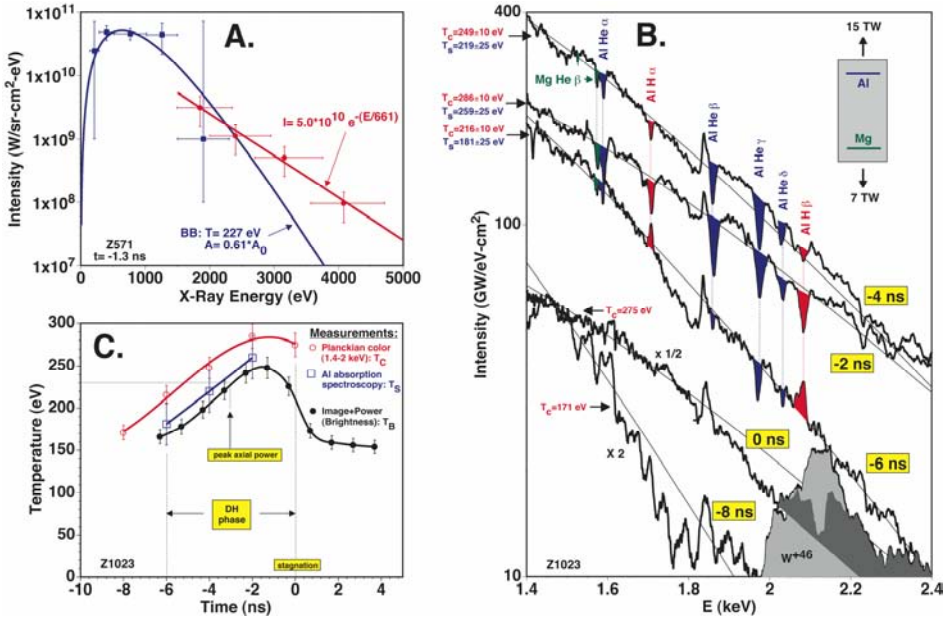

Figure 8. Measured top axial spectrum (A) near peak axial power and (B) between 1.4 and 2.4 keV, as a function of time. (C) Measured hohlraum temperature as a function of time, using three different techniques.

VIII. TOP-BOTTOM AXIAL RADIATION ASYMMETRY

A. More early tungsten observed from bottom than top REH

Surprisingly, measurements show the peak axial power exiting the top REH to be twice (2±0.5) that exiting the bottom REH [18], when the simple target shown in Fig. 2C is used with 2.4-mm-diameter REHs (see insert in Fig. 9A). The radiated energy, in contrast, is approximately the same from either end [18]. Because of the axial symmetry of the load about the target center (aside from the power feed) the power from each REH was expected to be identical [18]. Comparison of M-shell tungsten-emission features measured on GAMBLE II by Burkhalter [48] (insert in Fig. 9B) with simultaneous time-integrated features measured from both ends of the DH shows that significant tungsten emission originates from the bottom REH relative to that of the top (Fig. 9) [43]. The identifiable tungsten emission between 2.0 and 2.4 keV relative to the total emission measured between 1.4 and 3 keV is experimentally defined as the *tungsten fraction* (Fig. 9B) [43]. Top powers and associated tungsten fractions simultaneously measured for Shot Z1023 (which used the simple target), for example, are shown in Figs. 10A and 10B, respectively.

At early time, when power levels are low, tungsten is observed in both REHs, increasing more so in the bottom relative to the top REH as stagnation is approached. At stagnation and later times tungsten is observed in both REHs. Late-time tungsten is not a surprise, as by this time the tungsten shell crosses the REH and comes into the field of view of the axial detectors. By mounting the target on 3-mm high pedestals, the early-time tungsten is eliminated, and the powers and tungsten fractions nearly equalize

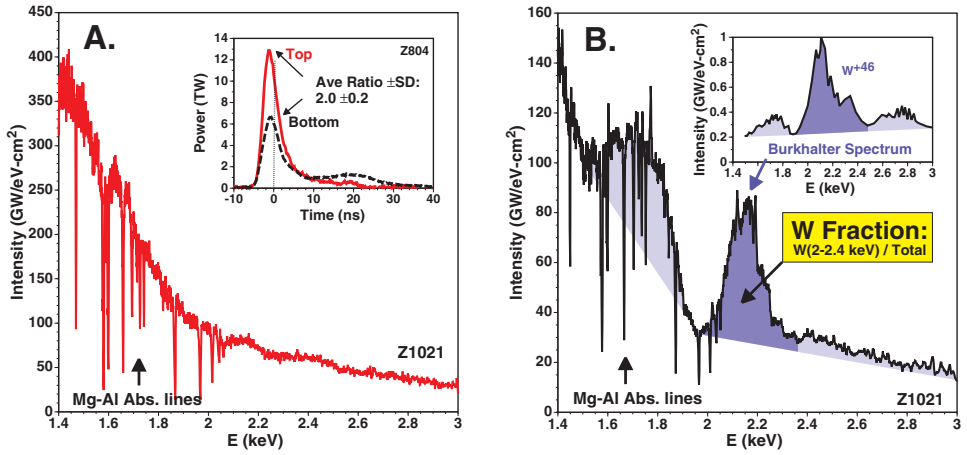

Figure 9. Time integrated spectra measured at (A) top and (B) bottom REH. Insert in (A) corresponds to top and bottom powers simultaneously measured useing 2.4-mm diameter REHs. Insert in (B) corresponds to M-shell tungsten spectrum measured by Burkhalter et al [48].

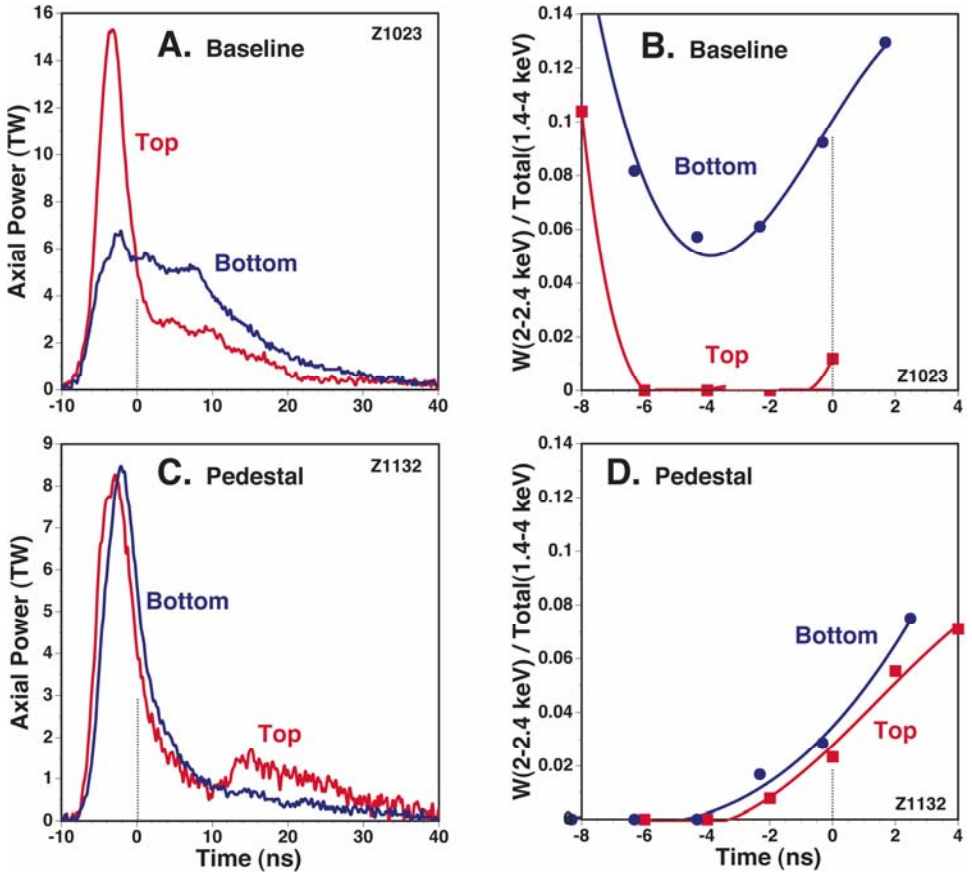

Figure 10. (A) Axial powers and (B) tungsten fractions measured using the simple target (Fig. 2C). (C) Axial powers and (D) tungsten fractions measured using the pedestal target (Fig. 2B).

(Figs. 10C and 10D) [43]. These results suggest that the early tungsten is localized near the electrodes. Hence it appears that the increased opacity near the REHs, resulting from this tungsten, is partially responsible for the reduction in power from the bottom REH relative to that of the top.

Figure 11A adds credence to this speculation, and shows that the peak axial power decreases monotonically with increased tungsten fraction at the time of peak power, independent of REH position, always with a greater tungsten fraction being present on the bottom relative to the top [43]. A three-component tungsten-temperature model [43] (see insert in Fig. 11B) is sufficient to simulate the power differences and spectral features. Specifically the model demonstrates that if ~2.5% of the initial tungsten mass were covering the bottom REH, this fraction would be sufficient to reduce the overall thermal emission from the DH interior by a factor of two, and be sufficient to generate the tungsten absorption (~2.0 keV) and emission (~2.2 keV) features seen above ~1.3 keV (Fig. 11B).

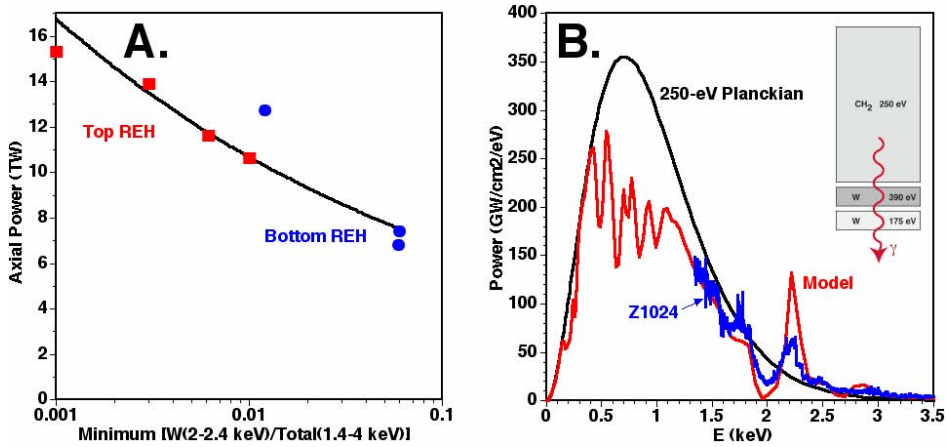

Figure 11. (A) Peak axial power measured as function of measured tungsten fraction at time of peak axial power. (B) Measured and simulated time-integrated spectrum using 3T Model illustrated in insert. 250 eV Planckian spectrum is also shown for reference.

The excess tungsten on the bottom relative to the top motivated the use of a single pedestal on the bottom cathode, when the top REH was used for high temperature radiation flow experiments [11]. Many shots like Z1577 of Fig. 12A, which had just a cathode pedestal, however, still show large top-bottom power asymmetries (Fig. 12B). Moreover, they often exhibit zippering of the main plasma shell at stagnation in x-ray streak-camera images, with the earliest arrival at the anode (Fig. 12A). Zippering results in top REH emission peaking earlier and with a faster rise time than emission from the bottom, and thus provides an additional contribution to the axial asymmetry. With two pedestals (Fig. 2B), the top-to-bottom power ratio decreased to 1.1±0.2. Even with both pedestals, however, the top emission generally occurs a bit earlier (Fig. 10C), with a slightly faster rise time (Fig. 10C) and with less tungsten fraction than the bottom (Fig. 10D) [43].

B. Origin of early tungsten

The origin of the early tungsten has been a mystery until now. With the large, widely varying asymmetry mitigated by the pedestals (of Fig. 2B) in the experiments discussed in Sections III and IV, however, we have been able to observe the radiation asymmetry more consistently as a function of one of the independent variables of the experiment, namely the radial electric field E_r (Fig. 2A) at the surface of the outer wires. This field is negative and near zero at the anode, because the cathode is held at negative high voltage relative to the anode and surrounding current cage (Fig. 2A). It is approximately given by the following expression, which was developed by Sasorov and is presented in Ref. [30]:

$$E_r = U z\Phi/\Delta l N\Phi_w \qquad (1)$$

where U is the voltage across the AK gap Δ (Fig. 2A), l and Φ are the length and diameter of the outer array, Φ_w and N are the diameter and

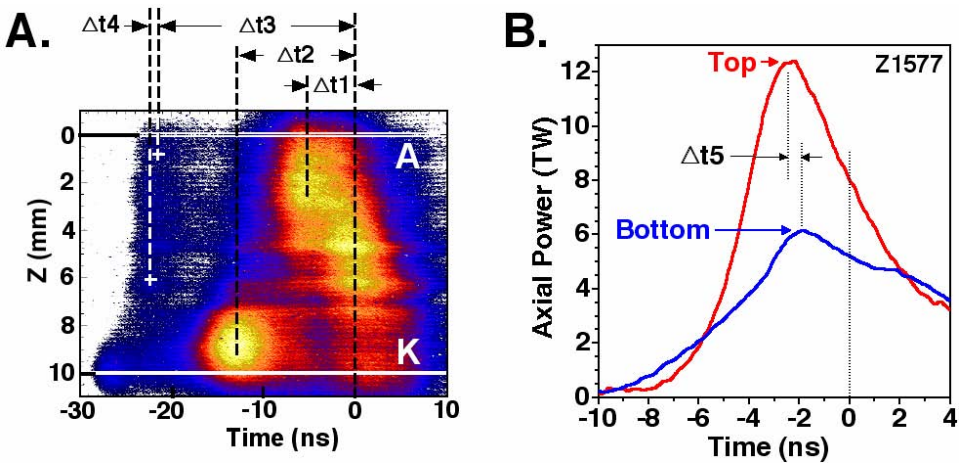

Figure 12. (A) X-ray streak camera image and (B) associated axial powers measured for Shot Z1577, which had a bottom pedestal only. Δt1= 4.7±0.5, Δt2= 14.6±2.0, Δt3= 21.7±1.4, and Δt4= 1.7±1.3 ns averaged over the four shots taken with this arrangement.

number of outer array wires, and *z* is measured from the anode (Fig. 12A).

The association of the asymmetry with E_r was motivated earlier [43] by the possible connection of the *polarity* effect in single wires first observed by Sarkisov [49] with the observation that the asymmetry greatly increases when the masses of the outer and inner wires are reversed relative to the baseline (Fig. 13). In this experiment (Section IV), the only change was to reduce the diameter of the outer wires Φ_w from 7.4 to 5.2 μm and increase the inner array wires from 7.4 to 11 μm. With this change, E_r increases a factor of 1.4 relative to the baseline (see Eq. 1 and Table I). Related effects are seen in Figs. 3A and 3C. In Fig. 3A, the larger the array diameter Φ, the larger E_r (see Eq. 1), and the larger the asymmetry. In Fig. 3C, the larger the wire number N, the smaller E_r (see Eq. 1), and the smaller the asymmetry.

When all the two-pedestal data (including those where Φ_w, Φ, and N were varied) are plotted as a function of E_r (Table I), the *relative* E_r appears to be a *unifying predictor of the asymmetry*, with higher E_r resulting in a larger range of asymmetry (Fig. 14). Above a relative E_r of ~0.8, the axial powers (Fig. 14A), the times of peak power (Fig. 14B), the rise times (Fig. 14C), and differences in the tungsten fractions (Fig. 14C) between top and bottom begin to diverge significantly. Here the relative E_r is defined to be the radial electric field at the midpoint (Fig. 2A) normalized by the field calculated for the baseline configuration, and is used as a dimensionless experimental parameter for correlating with the strength and timing of the axial asymmetry found in the x-ray emission.

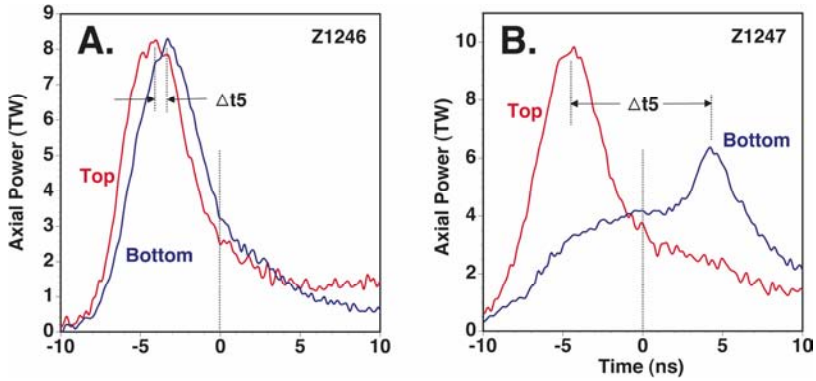

Figure 13. Axial powers measured for two sequential shots using (A) baseline and (B) mass reversed configurations. Both configurations used the pedestal target (Fig. 2B).

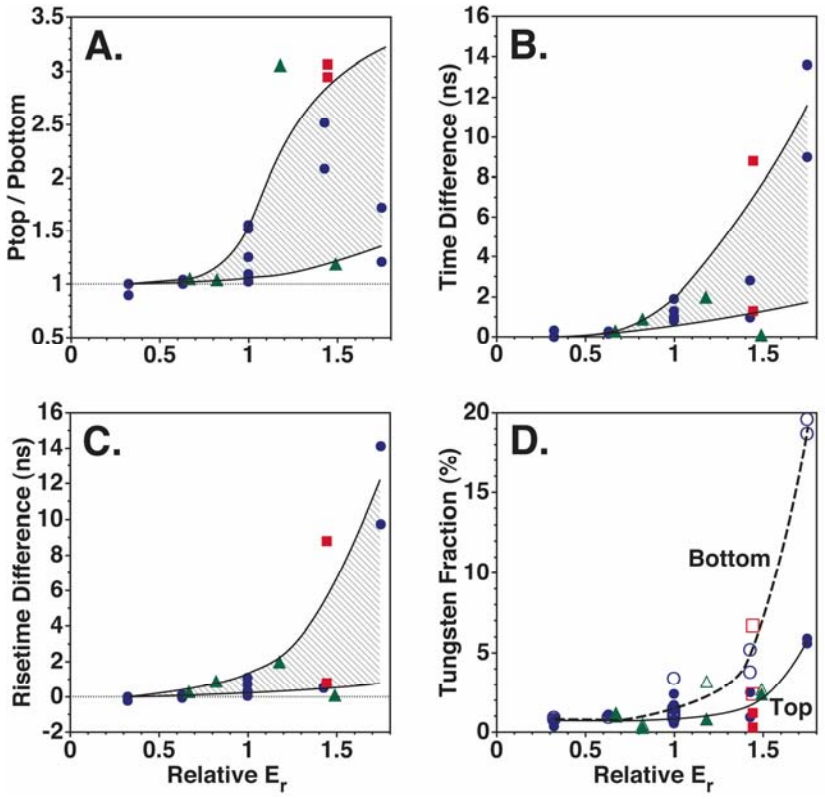

Figure 14. (A) Top-bottom power ratio at time of peak top axial power, (B) top-bottom peak-power time difference [Δt5 in Fig. 13], (C) top-bottom rise-time difference, and (D) top and bottom tungsten fractions versus relative E_r. Open data points in (D) correspond to bottom measurements. Circle, triangle, and square data correspond to array diameter, wire number, and mass-reversal scans (Table 1). The lines are only to help guide the eye [30].

This phenomenon may be understood as follows [30]. E_r (Fig. 15A) affects the current distribution at very early times when it can enhance electron emission from the wire cores and generate early breakdown of the vapor surrounding each wire (Fig. 15B). The current then shunts locally to this surrounding plasma of lower resistance, rather than remaining in the core. In this way, as found in single-wire experiments [49], the wire cores remain cold near the cathode and are not as hot, as near the anode. Therefore, for a given wire arrangement, the larger E_r (which is always near zero at the anode end of the pinch) becomes, the greater the energy-deposition imbalance between the top and bottom. The data of Fig. 14 thus suggest that the axial radiation asymmetry scales with axial energy-deposition variation.

C. Stagnation zipper

The zipper effect observed in Fig. 12A (Δt1) is now easily explained by this mechanism using the 3D resistive-MHD code GORGON [25]. Assuming an implosion of either hot or cold wires in the outer baseline array, the timing between when the hot wire array stagnates on axis is calculated to occur 4.0±0.5 ns earlier than when the cold-wire array stagnates (Δt1 in Fig. 16). This difference, symbolic of what occurs at either end of the z-pinch (Fig. 12A), is in agreement with the 4.7±0.5 ns measured for shots like those of Fig. 12. Specifically, the array with the lower initial temperature persists as a cold wire core, ablating material for a prolonged period of time before beginning to implode as a shell (Fig. 16). As the implosion proceeds, precursor tungsten contained within the array is snowplowed up, essentially tamping the acceleration of the imploding surface. This situation exemplifies what may occur near the

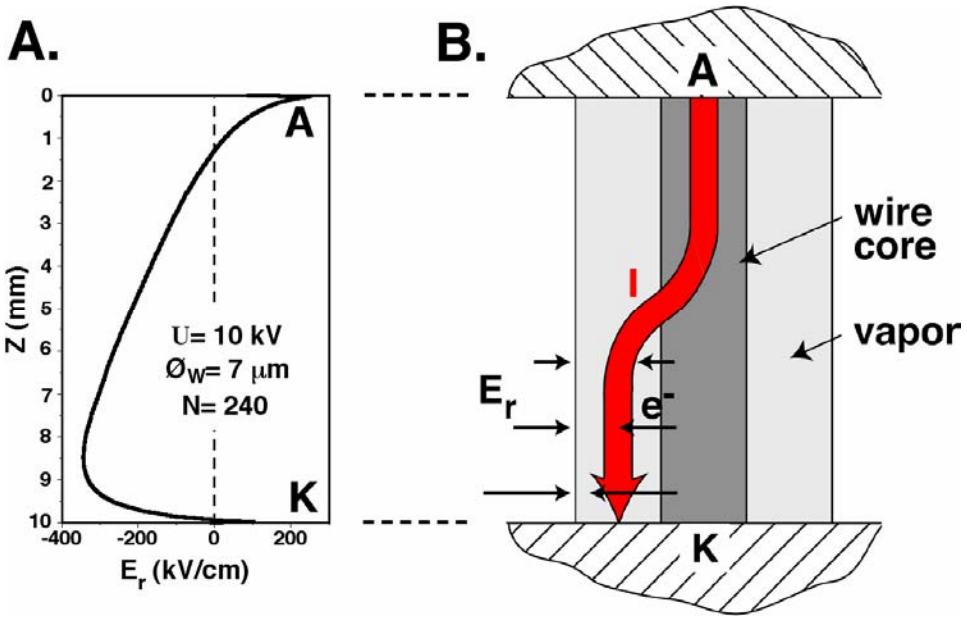

Figure 15. (A) Calculated radial electric field E_r at the surface of baseline outer wire array, and (B) illustration of current shunting from wire core to surrounding vapor when localized ionization occurs.

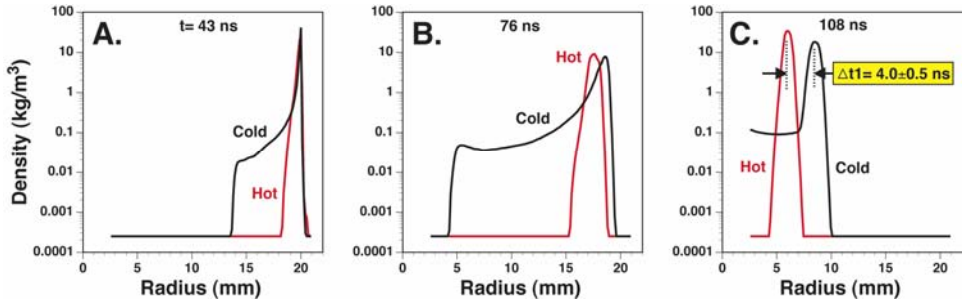

Figure 16. (A-C) Azimuthally averaged mass distributions flowing implosion of the 40-mm diameter baseline array for hot and cold initial core temperatures in GORGON [30].

cathode because of early current shunting (Fig. 15B). The precursor is partly blocked from reaching the z-axis by the bottom pedestal, which is responsible for the bright emission seen at z>7mm near -14 ns in Fig. 12 A.

For the high-initial-temperature array, which represents what may occur near the anode with little or no current shunting, the wire ablation proceeds more rapidly. The higher mass-ablation rate results in a lower velocity of ablated material and formation of little precursor material. Experimentally, little precursor plasma is seen at the anode. The core-corona structure does not persist for a prolonged period, and the implosion is more shell-like [19]. Between the ends, current shunting will gradually occur later as the anode is approached [49], resulting in the zippered stagnation of the main plasma shell, with the shell stagnating near the anode first.

D. Pre-stagnation zipper inverted

Prior to the shell stagnation, the early plasma precursor collides with the target (and pedestal) first near the cathode and later as the anode is approached, which results in the inverse-like zippered emission structure seen between -14 and -10 ns in Fig. 12A. Poor wire-electrode contact at the cathode enhances this effect [14]. It can lead to yet higher E_r fields in

the vicinity of the contact, where greater electron emission and earlier current shunting occurs, with the potential of arcing and localized heating of the wires (Fig. 17A).

The result is often increased early-time tungsten plasma flowing across the bottom REH [14]. This mechanism can again be simulated by GORGON, in this case by assuming a higher initial core temperature at the base of the array [44,50]. As the implosion proceeds, the increased ablation rate at the base results in the early implosion of this region. A magnetic bubble forms and blows through the bottom of the array, preceding the main implosion and potentially growing to a size that may exceed the 3-mm pedestal height (Fig. 17B). The maximum height to which the bubble grows is, however, limited by the current driving it, restriking across the gap it leaves behind. The growth of the bubble also has the effect of transporting mass upwards, thereby increasing the mass and hence de-accelerating the implosion surface immediately above the bubble.

This model predicts that the bubble will impact the pedestal 10±1 ns prior to the main shell (Δt2 in Fig. 12A), in reasonable agreement with the 14±2 ns measured. Moreover, the effect of the bubble (Fig. 18A) on the inner array is to transfer current to it prior to collision with the main shell (Fig. 18B), thus producing a ***JxB*** force that implodes the bottom of that array slightly earlier than its main body. This result is also observed in the streaked images (Fig. 12A). Emission from the collision of the outer array with the inner occurs 1.7±1.3 ns earlier on the cathode than on the anode (Δt4 in Fig. 12A). The 3D-GORGON simulations show that the bubble can be terminated before it expands vertically by indenting the cathode adjacent the current contact point [50], resulting in an axially homogeneous implosion at stagnation (Fig. 17C).

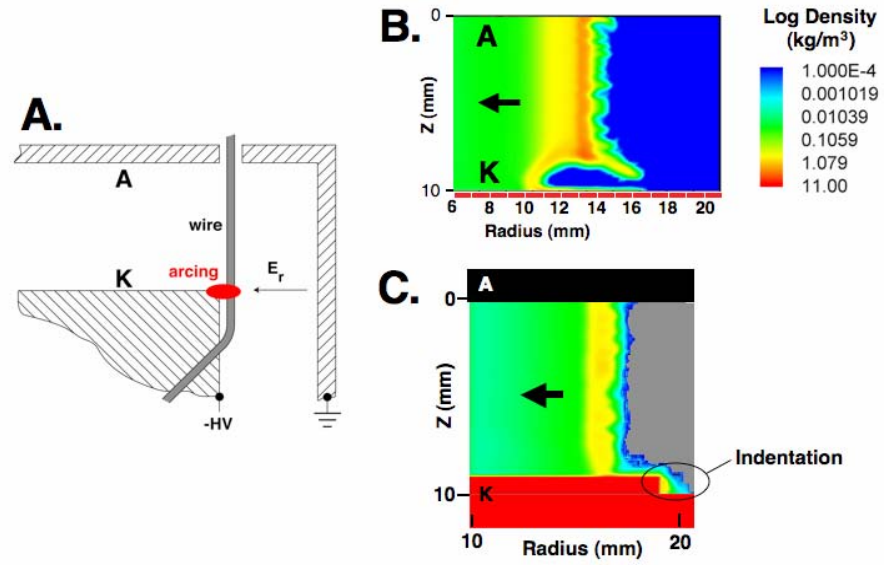

Figure 17. (A) Illustration of current shunting and associated arcing between the wires and cathode. Azimuthally averaged mass distributions of GORGON simulations of arcing (B) with no indentation, and (C) with indentation [50].

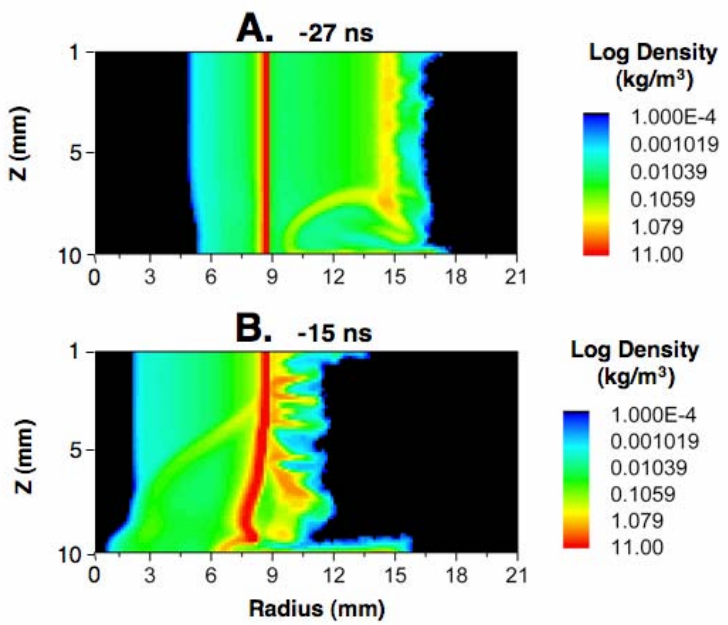

Figure 18. Azimuthally averaged mass distributions of GORGON simulations (A) prior to and (B) shortly after bubble impact with inner array [50]. Here the inner array was placed at ~9 mm.

IX. SUMMARY

The data and simulations reviewed here show the need to include the discrete nature of the wires, and the apertures in the current-return can, if a predictive capability is to be achieved. More specifically: (i) The decrease in axial power when the masses of the arrays are increased (Fig. 4B) is shown to be related to wire-number dynamics (Fig. 3C); (ii) the transparency of the inner wire array (Fig. 5) appears to account for the limited power gain by its inclusion (Fig. 4B); (iii) the measured azimuthal structure in the mass-driven shock in the target (Fig. 7) correlates with the azimuthal slot structure in the current return can (Fig. 2A); and (iv) wire initiation is shown to be central to the origin of axial top-bottom radiation asymmetry. This symmetry directly correlates with the magnitude of the negative radial electric field along the wire surface (Fig. 14), as estimated by Eq. (1). This field, in turn, is inferred to control the initial deposition of energy into the wire cores.

X. REFERENCES

[1] V. P. Smirnov, "Fast liners for inertial fusion", *Plasma Phys. Control. Fusion*, vol. 33, no.13, pp.1697-1714, Nov.1991.

[2] J. H. Brownell, R. L. Bowers, K. D. McLenithan, and D. L. Peterson, "Radiation environments produced by plasma z-pinch stagnation on central targets", *Phys. Plasmas*, vol. 5, no. 5, pp. 2071-2080, May 1998.

[3] T. J. Nash, M. S. Derzon, G. A. Chandler, R. Leeper, D. Fehl, J. Lash, C. Ruiz, G. Cooper, J. F. Seaman, J. McGurn, S. Lazier, J Torres, D. Jobe, T Gilliland, M. Hurst, R. Mock. P. Ryan, D. Nielsen, J. Armijo, J. McKenney, R. Hawn, and D. Hebron, "High-temperature dynamic hohlraums on the pulsed power driver Z", *Phys. Plasmas*, vol. 6, no. 5, pp. 2023-2029, May 1999.

[4] T. W. L. Sanford, T. J. Nash, R. E. Olson, D. E. Bliss, R. W. Lemke, C. L. Olson, C. L. Ruiz, R. C. Mock, J. E. Bailey, G. A. Chandler, M. E. Cuneo, R. J. Leeper, M. K. Matzen, T. A. Mehlhorn, S. A. Slutz, W. A. Stygar, D. L. Peterson, R. E. Chrien, R. E. Watt, N. F. Roderick, G. W. Cooper, J. P. Apruzese, G. S. Sarkisov, J. P. Chittenden, and M. G. Haines, "Progress in z-pinch driven dynamic-hohlraums for high-temperature radiation-flow and ICF experiments at Sandia National Laboratories", *Plasma Phys. Control. Fusion,* vol. 46, suppl. 12B, pp. B423-B433, Dec. 2004.

[5] T.W.L. Sanford, R.E. Olson, R. L. Bowers, G. A. Chandler, M. S. Derzon, D. E. Hebron, R. J. Leeper, R. C. Mock, T. J. Nash, D. L. Peterson, L. E. Ruggles, W. W. Simpson, K. W. Struve, and R. A. Vesey, "Z-pinch-generated X-rays demonstrate potential for indirect-drive ICF experiments.", *Phys. Rev. Lett.*, vol. 83, no. 26, pp. 5511-5514, Dec. 1999.

[6] T.W.L. Sanford, R.E. Olson, R.C. Mock, C. G. Chandler, R. J. Leeper, T. J. Nash, L. E. Ruggles, W. W. Simpson, K. W. Struve, D. L. Peterson, R. L. Bowers, W. Matuska, "Dynamics of a Z-pinch X-ray source for heating inertial-confinement-fusion relevant hohlraums to 120-160 eV, *Phys. Plasmas***,** vol. 7, no. 11, pp. 4669-4682, Nov. 2000.

[7] S. A. Slutz, J. E. Bailey, G. A. Chandler, G. R. Bennett, G. Cooper, J. S. Lash, S. Lazier, P. Lake, R. W. Lemke, T. A. Mehlhorn, T. J. Nash, D. S. Nielson, J. McGurn, T. C. Moore, C. L. Ruiz, D. G. Schroen, J. Torres, W. Varnum, R. A. Vesey, "Dynamic hohlraum driven inertial fusion capsules", *Phys. Plasmas*, vol. 10, no. 5, pp. 1875-1882, May 2003.

[8] J. E. Bailey, G. A. Chandler, S. A. Slutz, I. Golovkin, P. W. Lake, J. J. MacFarlane, R. C. Mancini, T. J. Burris-Mog, G. Cooper, R. J. Leeper, T. A. Mehlhorn, T. C. Moore, T. J. Nash, D. S. Nielsen, C. L. Ruiz, D. G. Schroen, and W. A. Varnum, "Hot dense capsule-implosion cores produced by Z-pinch dynamic hohlraum radiation", *Phys. Rev. Lett*., vol. 92, no. 8, pp. 085002/1-4, Feb. 2004.

[9] C. L. Ruiz, G. W. Cooper, S. A. Slutz, J.E. Bailey, G.A. Chandler, T.J. Nash, T. A. Mehlhorn, R. J. Leeper, D. Fehl, A. J. Nelson, J. Franklin, and L. Ziegler, "Production of Thermonuclear Neutrons from Deuterium-Filled Capsule Implosions Driven by Z-Pinch Dynamic Hohlraums ", *Phys. Rev. Lett.*, vol. 93, no. 1, 015001/1-4, Jul. 2004.

[10] T. W. L. Sanford, R. W. Lemke, R. C. Mock, G. A. Chandler, R. J. Leeper, C. L. Ruiz, D. L. Peterson, R. E. Chrien, G. C. Idzorek, R. G. Watt, J. P. Chittenden, *et. al*., "Dynamics and characteristics of a 215-eV dynamic-hohlraum x-ray source on Z". *Phys. Plasmas*, vol. 9, no. 8, pp. 3573-3594, Aug. 2002.

[11] R. G. Watt, R. E. Chrien, and G. Idzorek, "Investigation of radiation in a thin Au wall using x-ray backlit imaging", *Bull. Am. Phys. Soc*., vol. 48, p. 319, Oct. 2003.

[12] M. K. Matzen, M. A. Sweeney, R. G. Adams, ; J. R. Asay, J. E. Bailey, G. R. Bennett, D. E. Bliss, D. D. Bloomquist, T. A. Brunner, R. B. Campbell, G. A. Chandler, C. A. Coverdale, M. E. Cuneo, J. P. Davis, C. Deeney, M. P. Desjarlais, G. L. Donovan, C. J. Garasi, T. A. Haill, C. A. Hall, D. L. Hanson, M. J. Hurst, B. Jones, M. D. Knudson, R. J. Leeper, R. W. Lemke, M. G. Mazarakis, D. H. McDaniel, T. A. Mehlhorn, T. J. Nash, C. L. Olson, J. L. Porter, P. K. Rambo, S. E. Rosenthal, G. A. Rochau, L. E. Ruggles, C. L. Ruiz, T. W. L. Sanford, J. F. Seamen, D. B. Sinars, S. A. Slutz, I. C. Smith, K. W. Struve, W. A. Stygar, R. A. Vesey, E. A. Weinbrecht, D. F. Wenger, and E. P. Yu, "Pulsed-power-driven high energy density physics and inertial confinement fusion research.", *Phys. Plasmas*, vol. 12, no. 5, pp. 55503/1-16, May 2005.

[13] M. G. Haines, T. W. L. Sanford, and V. P. Smirnov, "Wire-array z-pinch: a powerful x-ray source for ICF", *Plasma Phys. Control. Fusion*, vol. 47, suppl. 12B, pp. B1-B11, Dec. 2005.

[14] T. W. L. Sanford, R. C. Mock, J. F. Seamen, M. R. Lopez, R. G. Watt, G. C. Idzorek, and D. L. Peterson, "Wire fixturing in high wire-number z pinches critical for high radiation power and reproducibility", *Phys. Plasmas*, vol. 12, pp. 122701/1-8, Dec. 2005.

[15] T. W. L. Sanford, T. J. Nash, R. C. Mock, J. P. Apruzese, and D. L. Peterson, "Diagnosed internal temperatures and shock evolution provide insight on dynamic-Hohlraum's axial radiation production and asymmetry", *Phys. Plasma*, vol. 13, pp. 022701/1-21, Jan. 2006.

[16] R. J. Leeper, T. E. Alberts, J. R. Asay, P. M. Baca, K. L. Baker, S. P. Breeze, G. A. Chandler, D. L. Cook, G. W. Cooper, C. Deeney, M. S. Derzon, M. R. Douglas, D. L. Fehl, T. Gilliland, D. E. Hebron, M. J. Hurst, D. O. Jobe, J. W. Kellogg, J. S. Lash, S. E. Lazier, T. K. Matzen, D. H. McDaniel, J. S. McGurn, T. A. Mehlhorn, A. R. Moats, R. C. Mock, D. J. Muron, T. J. Nash, R. E. Olson, J. L. Porter, J. P. Quintenz, P. V. Reyes, L. E. Ruggles, C. L. Ruiz, T. W. L. Sanford, F. A. Schmidlapp, J. F. Seamen, R. B. Spielman, M. A. Stark, K. W. Struve, W. A. Stygar, D. R. Tibbetts-Russell,J. A. Torres, M. Vargas, T. C. Wagoner, C. Wakefield, J. H. Hammer, D. D. Ryutov, M. Tabak, S. C. Wilks, R. L. Bowers, K. D. McLenithan, and D. L. Peterson, "Z pinch driven inertial confinement fusion target physics research at Sandia National Laboratories", *Nuclear Fusion* vol. 39, no. 9Y, pp. 1283-1294, Sep. 1999.

[17] R. E. Olson, G. A. Chandler, M. S. Derzon, D. E. Hebron, J. S. Lash, R. J. Leeper, T. J. Nash, G. E. Rochau, T. W. L. Sanford, N. B. Alexander, and C. R. Gibson, "Indirect-drive ICF target concepts for the X-1 Z-pinch facility", *Fusion Technol.*, vol. 35, no. 2, pp. 260-265, Mar. 1999.

[18] T. W. L. Sanford, R. C. Mock, R. J. Leeper, D. L. Peterson, R. C. Watt, R. E. Chrien, G. C. Idzorek, B. V. Oliver, N. F. Roderick, and M. G. Haines, "Unexpected axial asymmetry in radiated power from high-temperature dynamic-hohlraum x-ray sources", *Phys. Plasmas*, vol. 10, no. 5, pp. 1187-1190, May 2003.

[19] T. W. L. Sanford, G. O. Allshouse, B. M. Marder, T. J. Nash, R. C. Mock, R. B. Spielman, J. F. Seamen, J. C. McGurn, D. Jobe, T. L. Gilliland, M. Vargas, K. W. Struve, W. A. Stygar, M. R. Douglas M. K. Matzen, J. H. Hammer, J. S. DeGroot, J. L. Eddleman, D. L. Peterson, D. Mosher, K. G. Whitney, J. W. Thornhill, P. E. Pulsifer, J. P. Apruzese, and Y. Maron, "Improved symmetry greatly increases x-ray power from wire-array Z-pinches", *Phys. Rev. Lett.*, vol. 77, no. 25, pp. 5063-5066, Dec. 1996.

[20] T. W. L. Sanford, R. B. Spielman, G. O. Allshouse, G. A. Chandler, D. L. Fehl, W. A. Stygar, K. W. Struve, C. Deeney, T. J. Nash, J. F. Seamen, R. C. Mock, T. L. Gilliland, J. S. McGurn, and D. O. Jobe, "Wire number doubling in high-wire-number regime increases Z-accelerator X-ray power", *IEEE Trans. Plasma Sci.*, vol. 26, no. 4, pp. 1086-1093, Aug. 1998.

[21] D. L. Peterson, R. L. Bowers, J. H. Brownell, A. E. Greene, K. D. McLenithan, T. A. Oliphant, N. F. Roderick, and A. J. Scannapieco, "Two-dimensional modeling of magnetically driven Rayleigh-Taylor instabilities in cylindrical Z pinches", *Phys. Plasmas*, vol. 3, no. 1, pp. 368-381, Jan. 1996.

[22] D. L. Peterson, R. L. Bowers, K. D. McLenithan, C. Deeney, G. A. Chandler, R. B. Spielman, M. K. Matzen, and N. F. Roderick, "Characterization of energy flow and instability development in two-dimensional simulations of hollow z pinches", *Phys. Plasmas*, vol. 5, no. 9, pp. 3302-3310, Sep. 1998.

[23] D. L. Peterson, R. L. Bowers, W. Matuska, K. D. McLenithan, G. A. Chandler, C. Deeney, M. S. Derzon, M. Douglas, M. K. Matzen, T. J. Nash, R. B. Spielman, K. W. Struve, W. A. Stygar, and N. F. Roderick, "Insights and applications of two-dimensional simulations to Z-pinch experiments", *Phys. Plasmas*, vol. 6, no. 5, pp. 2178-2184, May 1999.

[24] J. P. Chittenden, S. V. Lebedev, S. N. Bland, A. Ciardi, and M. G. Haines, "The different dynamical modes of nested wire array Z pinches", *Phys. Plasmas*, vol. 8, no. 3, pp. 675-678, Mar. 2001.

[25] J. P. Chittenden, S. V. Lebedev, C. A. Jennings, S. N. Bland, and A. Ciardi, "X-ray generation mechanisms in three-dimensional simulations of wire array Z-pinches", *Plasma Phys. Control. Fusion*, vol. 46, suppl. 12B, SI, pp. B457-B476, Dec. 2004.

[26] S. V. Lebedev, R. Aliaga-Rossel, S. N. Bland, J. P. Chittenden, A. E. Dangor, M. G. Haines, and M. Zakaullah, "Two different modes of nested wire array z-pinch implosions", *Phys. Rev. Lett*., vol. 84, no. 8, 1708, Feb. 2000.

[27] D. B. Sinars, M. E. Cuneo, E. P. Yu, D. E. Bliss, T. J. Nash, J. L. Porter, C. Deeney, M. G. Mazarakis, G. S. Sarkisov, and D. F. Wenger, "Mass-profile and Iinstability-growth measurements for 300-wire z-pinch implosions driven by 14–18 MA", *Phys. Rev. Lett.,* vol. 93, no. 14, pp. 145002/1-4, Oct. 2004.

[28] M. E. Cuneo, D. B. Sinars, D. E. Bliss, E. M. Waisman, J. L. Porter, W. A. Stygar, S. V. Lebedev, J. P. Chittenden, G. S. Sarkisov, and B. B. Afeyan, "Direct experimental evidence for current-transfer mode operation of nested tungsten wire arrays at 16–19 MA", *Phys. Rev. Lett.*, vol 94, no. 22 pp. 225003/1-4, Jun. 2005.

[29] T. W. L. Sanford, R. W. Lemke, R. C. Mock, and D. L. Peterson , "Trends in radiation production from dynamic-hohlraums driven by single and nested wire arrays", *Phys. Plasmas*,vol. 10, no. 8, pp. 3252-3264, Aug. 2003.

[30] T. W. L. Sanford, C. A. Jennings, G. A. Rochau, S. E. Rosenthal, G. S. Sarkisov, P. V. Sasorov, W. A. Stygar, L. F. Bennett, D. E. Bliss, J. P. Chittenden, M. E. Cuneo, M. G. Haines, R. J. Leeper, R, C. Mock, T. J. Nash, and D. L. Peterson, "Wire initiation critical for radiation symmetry in z-pinch–driven dynamic hohlraums, *Phys. Rev. Lett*., vol 98, no. 6, pp. 065003/1-4, Feb. 2007.

[31] R. B. Spielman, C. Deeney, G. A. Chandler, M. R. Douglas, D. L. Fehl, M. K. Matzen, D. H. McDaniel, T. J. Nash, J. L. Porter, T. W. L. Sanford, J. F. Seamen, W. A. Stygar, K. W. Struve, S. P. Breeze, J. S. McGurn, J. A. Torres, D. M. Zagar, T. L. Gilliland, D. O. Jobe, J. L. McKenney, R. C. Mock, M. Vargas, T. Wagoner, and D. L. Peterson, "Tungsten wire-array z-pinch experiments at 200 TW and 2 MJ*, Phys. Plasmas*, vol. 5, no. .5, pp. 2105-11, May 1998.

[32] K. W. Struve, T. H. Martin, R. B. Spielman, W. A. Stygar, P. A. Corcoran, and J. W. Douglas, "Circuit-code modeling of the PBFA Z for z-pinch experiments", *11th IEEE Inter. Pulse Power Conf*., Baltimore MD, Digest of Technical Papers (Jun. 29 - Jul. 2, 1997), edited by G. Cooperstein and I. Vitkovititsky, IEEE cat. no. 97CH36127, vol. 1, pp. 162-167, 1997.

[33] T. J. Nash, T. W. L. Sanford, and R. C. Mock, "Current scaling of axially radiateed power in dynamic hohlraums and dynamic hohlraum load design for ZR", Sandia National Laboratories technical report SAND 2007-0992, Mar. 2007.

[34] M. G. Mazarakis, C. E. Deeney, M. R. Douglas, W. A. Stygar, D. B. Sinars, M. E. Cuneo, J, Chittenden, G. A. Chandler, T. J. Nash, K. W. Struve and D. H. McDaniel, "Tungsten wire number

dependence of the implosion dynamics at the Z-accelerator". *Plasma Devices and Operations*, vol. 3, no. 2, pp. 157-161, June 2005.

[35] C. A. Coverdale, C. Deeney, M. R. Douglas, J. P. Apruzese, K. G. Whitney, J. W. Thornhill, and J. Davis, "Optimal wire-number range for high x-ray power in long-implosion-time aluminum Z pinches", *Phys. Rev. Lett*., vol. 88, no. 6, pp. 065001/1-4, Feb. 2002.

[36] M. E. Cuneo, E. M. Waisman, S. V. Lebedev, J. P. Chittenden, W. A. Stygar, G. A. Chandler, R. A. Vesey, E. P. Yu, T. J. Nash, D. E. Bliss, G. S. Sarkisov, T. C. Wagoner, G. R. Bennett, D. B. Sinars, J. L. Porter, W. W. Simpson, L. E. Ruggles, D. F. Wenger, C. J. Garasi, B. V. Oliver, R. A. Aragon, W. E. Fowler, M. C. Hettrick, G. C. Idzorek, D. Johnson, K. Keller, S. E. Lazier, J. S. McGurn, T. A. Mehlhorn, T. Moore, D. S. Nielsen, J. Pyle, S. Speas, K. W. Struve, and J. A. Torres, "Characteristics and scaling of tungsten-wire-array z-pinch implosion dynamics at 20 MA", *Phys. Rev. E*, vol. 71, no. 4, pt. 2, pp. 046406/1-43, Apr. 2005.

[37] G. M. Oleinik, V. V. Alexandrov, I. N. Frolov, E. V. Grabovsky, A. N. Gribov, K. N. Mitrofanov, I. Y. Porofeev, A. A. Samokhin, V. P. Smirnov, P. V. Sasorov, G. S. Sarkisov, and K. W. Struve, "Influence of a radial electrical field on implosion of wire array"*, J. Phys. IV* (France), vol. 133; pp. 779-781, June 2006.

[38] T. W. L. Sanford, M. E. Cuneo, D. E. Bliss, C. A. Jennings, R. C. Mock, T. J. Nash, W. A. Stygar, E. M. Waisman, J. P. Chittenden, M. G. Haines, and D. L. Peterson, "Demonstrated transparent mode in nested wire-arrays used for Dynamic Hohlraum Z-pinches", to be published *Phys. Plasmas*, Febuary 2007.

[39] E. M. Waisman, M. E. Cuneo, W. A. Stygar, R. W. Lemke, K. W. Struve, and T. C. Wagoner, "Wire array implosion characteristics from determination of load inductance on the Z pulsed-power accelerator", *Phys. Plasmas*, vol. 11, no. 5, pp. 2009-2013, May 2004.

[40] M. E. Cuneo, R. A. Vesey, D. B. Sinars, J. P. Chittenden, E. M. Waisman, R. W. Lemke, S. V. Lebedev, D. E. Bliss, W. A. Stygar, J. L. Porter, D. G. Schroen, M. G. Mazarakis, G. A. Chandler, and T. A. Mehlhorn, "Demonstration of radiation pulse shaping with nested-tungsten-wire-array Z pinches for high-yield inertial confinement fusion, *Phys. Rev. Lett.,* vol. 95, no. 18, pp. 185001/1-4, Oct. 2005.

[41] M. E. Cuneo, D. B. Sinars, E. M. Waisman, D. E. Bliss, W. A. Stygar, R. A. Vesey, R. W. Lemke, I. C. Smith, P. K. Rambo, J. L. Porter, G. A. Chandler, T. J. Nash, M. G. Mazarakis, R. G. Adams, E. P. Yu, K. W. Struve, T. A. Mehlhorn, S. V. Lebedev, J. P. Chittenden, and C. A. Jennings, "Compact single and nested tungsten-wire-array dynamics at 14-19 MA and applications to inertial confinement fusion", *Phys. Plasmas*, vol. 13, no. 5, pp. 56318/1-18, May 2006.

[42] T. W. L. Sanford, R. C. Mock, S. A. Slutz, and D. L. Peterson, "Length scaling of dynamic-hohlraum axial radiation", *Phys. Plasmas*, vol. 10, no. 12, pp. 4790-4799, Dec. 2003.

[43] T. W. L. Sanford, T. J. Nash, R. C. Mock, D. L. Peterson, R. G. Watt, R. E. Chrien, J. P. Apruzese, R. W. Clark, N. F. Roderick, G. S. Sarkisov, and M. H. Haines, "Evidence and mechanisms of axial-radiation asymmetry in dynamic hohlraums driven by wire-array Z pinches", *Phys. Plasmas*, vol. 12, no. 2, pp. 22701/1-15, Feb. 2005.

[44] J. P. Chittenden, private communication, Apr. 2006.

[45] J. P. Apruzese, R. W. Clark, P. C. Keppe, J. Davis, T. W. L. Sanford, T. J. Nash, R. C. Mock, and D. L. Peterson, "Diagnosing dynamic hohlraums with tracer absorption line spectroscopy", *Phys. Plasmas*, vol. 12, no. 1, pp. 12705/1-8, Jan. 2005.

[46] J. P. Apruzese, R. W. Clark, J. Davis, T. W. L. Sanford, T. J. Nash, R. C. Mock, and D. L. Peterson, "Diagnosing the properties of dynamic Hohlraums with tracer spectroscopy (invited)", *Re. Sci. Instrum.*, vol. 77, no. 10, pp. 10F303/1-4, Oct. 2006.

[47] J. P. Apruzese, R. W. Clark, P. C. Keppe, *et al* , "Comparative properties of the interior and blow-off plasma in a dynamic hohraum", to be published *Phys. Plasmas*, Apr. 2007.

[48] P. G. Burkhalter, C. M. Dozier, and D. J. Nagel, "X-ray-spectra from exploded-wire plasmas", *Phys. Rev. A*, vol. 15, no. 2, pp. 700-717, 1977.

[49] G. S. Sarkisov, P. V. Sasorov, K. W. Struve, D. H. McDaniel, A. N. Gribov, and G. M. Oleinik, "Polarity effect for exploding wires in a vacuum", *Phys. Rev. E*, vol. 66, no. 4, pt. 2, pp. 046413/1-6, Oct. 2002.

[50] C. A. Jennings, private communication, May 2006.

Distribution

External:

1 Professor Jeremy Chittenden
Plasma Physics Group, Blackett Laboratories
Prince Consort Rd
South Kennsington, London
SW72BZ
UK

1 Professor Malcolm Haines
Plasma Physics Group, Blackett Laboratories
Prince Consort Rd
South Kennsington, London
SW72BZ
UK

1 Professor Sergey Lebedev
Plasma Physics Group, Blackett Laboratories
Prince Consort Rd
South Kennsington, London
SW72BZ
UK

1 Dr. Simon Bland
Imperial College London
South Kensington Campus, London
SW72AZ
UK

1 Professor David Hammer
327 Rhodes Hall
Cornell University
Ithaca, NY 14853

1 Dr. Darrell Peterson
Los Alamos National Laboratory
P.O. Box 1663
Los Alamos, NM 87545

1 Dr. Robert Watt
Los Alamos National Laboratory
P.O. Box 1663
Los Alamos, NM 87545

Internal:

1	MS 0104	T. C. Bickel, 1200
2	MS 0123	D. L. Chavez, 1011
1	MS 0125	J. P. VanDevender, 12101
1	MS 0125	F. L. Vook, 12101
1	MS 0511	J. E. Maenchen, 1212
1	MS 0839	G. Yonas, 7000
1	MS 1106	D. Ampleford, 1673
1	MS 1129	R. E. Nygren, 1658
1	MS 1152	M. L. Kiefer, 1652
1	MS 1152	L. P. Mix, 1652
1	MS 1152	T. D. Pointon, 1652
1	MS 1152	D. B. Seidel, 1652
1	MS 1152	M. Caldwell, 1653
1	MS 1159	J. W. Bryson, 1344
1	MS 1159	C. A. Coverdale, 1344
1	MS 1159	V. Harper-Slaboszewicz, 1344
1	MS 1168	C. A. Hall, 1646
1	MS 1168	D. H. McDaniel, 1650
1	MS 1168	B. M. Jones, 1673
1	MS 1168	P. D. LePell, 1673
1	MS 1169	J. R. Lee, 1300
1	MS 1178	D. D. Bloomquist, 1630
1	MS 1178	E. A. Weinbrecht, 1635
1	MS 1178	F. W. Long, 1637
1	MS 1178	L. G. Baldwin, 1639
1	MS 1178	G. R. McKee, 1639
1	MS 1178	D. A. Muirhead, 1639
1	MS 1178	D. L. Smith, 1639
1	MS 1178	G. L. Donovan, 1676
1	MS 1181	T. A. Mehlhorn, 1640
1	MS 1181	J. R. Asay, 1646
1	MS 1181	M. D. Knudson, 1646
1	MS 1181	L. C. Chhabildas, 1647
1	MS 1181	L. X. Schneider, 1650
1	MS 1186	M. P. Desjarlais, 1640
1	MS 1186	T. A. Brunner, 1641
1	MS 1186	R. B. Campbell, 1641
1	MS 1186	K. R. Cochrane, 1641
1	MS 1186	C. J. Garasi, 1641
1	MS 1186	T. A. Haill, 1641
1	MS 1186	H. L. Hanshaw, 1641
1	MS 1186	C. Jennings, 1641
1	MS 1186	R. W. Lemke, 1641
1	MS 1186	E. P. Yu, 1641
1	MS 1186	J. F. Seamen, 1670
1	MS 1186	P. J. Christenson, 1674
1	MS 1186	M. Herrmann, 1674
1	MS 1186	J. J. MacFarlane, 1674

1	MS 1186	K. Peterson, 1674
1	MS 1186	S. E. Rosenthal, 1674
1	MS 1186	S. A. Slutz, 1674
1	MS 1186	R. A. Vesey, 1674
1	MS 1186	R. C. Mancini, 1677
1	MS 1190	M. K. Matzen, 1600
1	MS 1190	C. L. Olson, 1640
1	MS 1191	M. M. Sluyter, 1600
1	MS 1191	D. O. Jobe, 1670
1	MS 1191	J. L. Porter, 1670
1	MS 1191	M. A. Sweeney, 1670
1	MS 1192	M. L. Harris, 1676
1	MS 1192	J. A. Mills, 1676
1	MS 1192	G. S. Sarkisov, 1676
1	MS 1192	J. J. Seamen, 1676
1	MS 1193	K. R. Prestwich, 1645
1	MS 1193	D. C. Rovang, 1645
1	MS 1193	P. W. Spence, 1645
1	MS 1193	D. R. Welch, 1645
1	MS 1193	J. P. Corley, 1671
1	MS 1193	D. J. Johnson, 1671
1	MS 1193	J. R. Woodworth, 1671
1	MS 1193	B. W. Atherton, 1672
1	MS 1193	G. R. Bennett, 1672
1	MS 1193	J. E. Potter, 1672
1	MS 1193	M. E. Cuneo, 1673
1	MS 1193	D. L. Hanson, 1673
1	MS 1193	D. B. Sinars, 1673
1	MS 1193	G. T. Leifeste, 1675
1	MS 1193	M. R. Lopez, 1675
1	MS 1193	L. E. Ruggles, 1675
1	MS 1193	M. F. Vargas, 1675
1	MS 1193	D. F. Wenger, 1675
1	MS 1194	L. F. Bennett, 1671
1	MS 1194	D. E. Bliss, 1671
1	MS 1194	M. G. Mazarakis, 1671
1	MS 1194	M. E. Savage, 1671
1	MS 1194	K. W. Struve, 1671
1	MS 1194	E. M. Waisman, 1673
1	MS 1194	T. C. Wagoner, 1676
1	MS 1196	A. L. Carlson, 1675
1	MS 1196	D. S. Nielsen, 1675
1	MS 1196	J. E. Bailey, 1677
1	MS 1196	G. A. Chandler, 1677
1	MS 1196	G. W. Cooper, 1677
1	MS 1196	G. S. Dunham, 1677
1	MS 1196	D. L. Fehl, 1677
1	MS 1196	R. J. Leeper, 1677
1	MS 1196	R. C. Mock, 1677
1	MS 1196	T. J. Nash, 1677
1	MS 1196	R. E. Olson, 1677
1	MS 1196	G. A. Rochau, 1677
1	MS 1196	C. L. Ruiz, 1677
20	MS 1196	T. W. L. Sanford, 1677
1	MS 1196	W. A. Stygar, 1677
1	MS 1196	J. A. Torres, 1677
2	MS 9018	Central Technical Files, 8944
2	MS 0899	Technical Library, 4536